# Separation of Vortex Shedding Tones and Broadband Signals using SPOD of uPSP Measurements in NASA Ames Wind Tunnel Test

Jie Li[1], E. Lara Lash[2], Kenneth R. Lyons[2], David D. Murakami[2], Nettie H. Roozeboom[2], Marc A. Shaw-Lecerf[2], Evan D. Crowe[1], Nathan W.C. Eller[2], Sofia Y. Tafolla[2]

[1]Metis Technology Solutions, Inc.
*Moffett Field, CA 94035*

[2] NASA Ames Research Center
*Moffett Field, CA 94035*

**This paper discusses the outputs of Spectral Proper Orthogonal Decomposition (SPOD) of Unsteady Pressure-Sensitive Paint (uPSP) measurements in a Space Launch System (SLS) Force & Moment Test. The uPSP measurements were collected in the transonic wind tunnel with a scale mode of the SLS Block 1 crew vehicle at NASA Ames Research Center in April 2025. Vortex shedding tones, which were generated by the forward attachments of the Solid Rocket Boosters (SRBs) were consistently observed in the uPSP measurements. In this paper, it is demonstrated, with SPOD and Inverse SPOD, the original uPSP measurements are effectively separated into two datasets of timeseries of the vortex shedding tones and broadband signals. The characteristics of the vortex shedding tones are presented through visualization of the SPOD modes. The work described in this paper is a part of NASA's development of a new state-of-the-art uPSP capability in production wind tunnels.** **Funding was provided by the NASA Aerosciences Evaluation and Test Capabilities Portfolio Office of the Aeronautics Research Mission Directorate.**

## Nomenclature

| | |
|---|---|
| CSD | = Cross Spectral Density |
| DFT | = Discrete Fourier Transform |
| DMD | = Dynamic Mode Decomposition |
| ISSI | = Innovative Scientific Solutions, Inc. |
| PSD | = Power Spectral Density |
| SLS | = Space Launch System |
| SPOD | = Spectral Proper Orthogonal Decomposition |
| SRB | = Solid Rocket Booster |
| uPSP | = Unsteady Pressure-Sensitive Paint |
| UPWT | = NASA Unitary Plan Wind Tunnel |
| $\mathbb{C}$ | = set of complex numbers |
| $\hat{C}_m$ | = estimated CSD matrix at the frequency $f_m$ |
| $f_{binWidth}$ | = bin width of DFT, showing the frequency resolution |
| $f_m$ | = frequency corresponding to the vectors $\hat{q}_{uPSP,m}^{(k)}$ and $\hat{q}_{VS,m}^{(k)}$ |
| $f_{sample}$ | = sample frequency of the uPSP measurements |
| $I_{N_{mode}\times N_{mode}}$ | = identity matrix of the dimension $N_{mode} \times N_{mode}$ |
| $\tilde{M}_m$ | = Hermitian matrix defined for a computational shortcut to solve for SPOD modes |
| $N_{block}$ | = number of blocks |
| $N_{DFT}$ | = number of frames in a block, i.e., the length of DFT |
| $N_{frame}$ | = number of frames |
| $N_{mode}$ | = number of SPOD modes of the original uPSP measurements |
| $N_{mode,VS}$ | = number of dominant SPOD modes of the vortex shedding tones |
| $N_{node}$ | = number of selected grid nodes |

$Q_{BB}$ = matrix of the full timeseries of the broadband signals on the selected grid nodes

$Q_{uPSP}$ = matrix of the full timeseries of the original uPSP measurements on the selected grid nodes

$Q_{uPSP}^{(k)}$ = matrix of the original uPSP measurements in the $k$-th block on the selected grid nodes, $k = 1, 2, \dots, N_{block}$

$\hat{Q}_{uPSP}^{(k)}$ = DFT of the matrix $Q_{uPSP}^{(k)}$

$\hat{q}_{uPSP,m}^{(k)}$ = $k$-th column of the matrix $\hat{X}_{uPSP,m}$, also $m$-th column of the matrix $\hat{Q}_{uPSP}^{(k)}$, $m = 1, 2, \dots, N_{DFT}$, $k = 1, 2, \dots, N_{block}$

$q_{uPSP,s}^{(k)}$ = $s$-th column of the matrix $Q_{uPSP}^{(k)}$, $s = 1, 2, \dots, N_{DFT}$

$q_{uPSP,t}$ = $t$-th column of the matrix $Q_{uPSP}$, $t = 1, 2, \dots, N_{frame}$

$Q_{VS}$ = matrix of the full timeseries of the vortex shedding tones on the selected grid nodes

$Q_{VS}^{(k)}$ = matrix of the vortex shedding tones in the $k$-th block on the selected grid nodes, $k = 1, 2, \dots, N_{block}$

$\hat{Q}_{VS}^{(k)}$ = DFT of the matrix $Q_{VS}^{(k)}$

$\hat{q}_{VS,m}^{(k)}$ = $k$-th column of the matrix $\hat{X}_{VS,m}$, also $m$-th column of the matrix $\hat{Q}_{VS}^{(k)}$, $m = 1, 2, \dots, N_{DFT}$, $k = 1, 2, \dots, N_{block}$

$\mathbb{R}$ = set of real numbers

$\hat{X}_{uPSP,m}$ = matrix of the frequency components of the original uPSP measurements in all blocks on the selected grid nodes at the frequency $f_m$

$\hat{X}_{VS,m}$ = matrix of the frequency components of the vortex shedding tones in all blocks on the selected grid nodes at the frequency $f_m$, generated from dominant SPOD modes of the vortex shedding tones

$\Lambda_m$ = matrix of eigenvalues of the matrix $\hat{C}_m$

$\lambda_{m,i}$ = $i$-th eigenvalue of the matrix $\hat{C}_m$ arranged in descending order, $i = 1, 2, \dots, N_{mode}$

$\hat{\Phi}_m$ = matrix of eigenvectors of the matrix $\hat{C}_m$

$\hat{\phi}_{m,i}$ = eigenvector of the matrix $\hat{C}_m$ corresponding to $\lambda_{m,i}$

$\hat{\Psi}_m$ = matrix of eigenvectors of the matrix $\hat{M}_m$

$\hat{\psi}_{m,i}$ = eigenvector of the matrix $\hat{M}_m$ corresponding to $\lambda_{m,i}$

$(\cdot)^*$ = conjugate transpose

**Notice to Readers**

Certain features and characteristics of the Space Launch System vehicle are defined by the U.S. Government as Export-Controlled, Controlled Unclassified Information (CUI). To comply with CUI restrictions, values in some plots and figures have been either removed or normalized to arbitrary values. It is the opinion of the authors that these alternations do not detract from the relevant technical discussions.

## I. Introduction

This paper discusses the separation of the vortex shedding tones and the broadband signals using Spectral Proper Orthogonal Decomposition (SPOD) of the Unsteady Pressure-Sensitive Paint (uPSP) measurements in the wind tunnel tests of the Space Launch System (SLS) vehicle at NASA Ames Research Center. The characteristics of the vortex shedding tones, generated by the forward attachments of the Solid Rocket Boosters (SRBs) of the launch vehicle, are presented through visualization of the SPOD modes.

The uPSP measurements were collected using Innovative Scientific Solutions, Inc. (ISSI) Porous, Fast-Response Pressure-Sensitive Paint (FP-XXX) [1], 40 ISSI four-inch air-cooled light-emitting diodes, and 8 Phantom v2512 high-speed cameras at 10,000 frames per second in a Force & Moment Test of the SLS Block 1 crew vehicle in the 11-by 11-ft transonic test section of the Unitary Plan Wind Tunnel (UPWT) at NASA Ames Research Center in April 2025. Figure 1 shows the scale model of the SLS Block 1 crew vehicle installed in the wind tunnel with uPSP applied to the model surface.

The vortex shedding tones generated from the forward attachments of the SRBs were consistently observed in the uPSP measurements of the SLS Force & Moment Test. As an example, Fig. 2 shows a mode of Dynamic Mode Decomposition (DMD) of the uPSP measurements at the frequency of the vortex shedding tone in the supersonic test at Mach number 1.20. [2, 3] In this paper, the outputs of SPOD of the uPSP measurements on the selected grid nodes in the neighboring areas of the forward attachments of the SRBs are presented. The two red boxes in Fig. 2 illustrate the areas of the selected grid nodes.

SPOD [4-6] can be viewed as an extension of DMD and is derived from a space-time proper orthogonal decomposition problem for statistically stationary flows. SPOD modes are determined in the frequency domain. Each SPOD mode oscillates at a single frequency. SPOD of uPSP measurements consists of two steps: (1) the full timeseries of uPSP measurements are partitioned into a set of smaller blocks, and each block is converted from the time domain to the frequency domain with the Discrete Fourier Transform (DFT); (2) at each frequency, the Cross Spectral Density (CSD) matrix is estimated with Welch's method, and the SPOD modes are determined as the eigenvectors of the estimated CSD matrix and arranged in the descending order of the corresponding eigenvalues.

In a previous paper, the SPOD outputs of the uPSP measurements were presented and the effectiveness of SPOD in the identification, diagnosis and analysis of the aerodynamic and aeroacoustic phenomena was demonstrated [7]. In this paper, it is demonstrated the vortex shedding tones can be effectively separated from the broadband signals in the time domain using the Inverse SPOD of the dominant SPOD modes revealing the characteristics of the vortex shedding tones.

From the datasets of timeseries of the vortex shedding tones and broadband signals, the timeseries of average pressures were generated on patches for the structural dynamics analysis of the SLS launch vehicle. The separated vortex shedding tones and broadband signals can also be used in the diagnosis and analysis of the pressure field on the surface of the SLS launch vehicle. For example, the broadband signals, with the vortex shedding tones removed, can be used in the extraction of parameters of the Corcos model in the estimation of the Buffet Forcing Functions of the SLS launch vehicle [8]. The bulk convection speed can be estimated at a better accuracy with the separated vortex shedding tones.

The work described in this paper is a part of NASA's development of a new state-of-the-art uPSP capability in production wind tunnels. For more work on uPSP at NASA, please see Refs. [9-19]. The uPSP measurements were processed with the uPSP data processing software, which was described in detail by Powell, et al. [20] and Shaw-Lecerf, et al. [21] The software used to generate the SPOD outputs and the timeseries of vortex shedding tones and broadband signals makes use of the open-source packages *SPOD* [5, 22] in MATLAB and *PySPOD* [23] in Python.

## II. SPOD and Inverse SPOD Algorithms

In this section, the algorithms of SPOD and Inverse SPOD, which are used to generate the outputs of SPOD of the original uPSP measurements and separate the vortex shedding tones from the broadband signals, are described. More detailed descriptions of the algorithms of SPOD and Inverse SPOD are given in Refs. [4-6].

### A. uPSP Data in Blocks

The SPOD algorithm consists of two steps. In the first step, the full timeseries of the uPSP measurements are partitioned into a set of smaller blocks.

Let $N_{node}$ be the number of selected grid nodes and $N_{frame}$ be the number of frames, the full timeseries of original uPSP measurements on the selected grid nodes can be written as an $N_{node} \times N_{frame}$ matrix of real numbers

$$Q_{uPSP} = [q_{uPSP,1} \quad q_{uPSP,2} \quad \cdots \quad q_{uPSP,t} \quad \cdots \quad q_{uPSP,N_{frame}}] \tag{1}$$

where $Q_{uPSP} \in \mathbb{R}^{N_{node} \times N_{frame}}$, $q_{uPSP,t} \in \mathbb{R}^{N_{node}}$, $t = 1, 2, \ldots, N_{frame}$. $\mathbb{R}$ is the set of real numbers.

Let $N_{DFT}$ be the number of frames in a block, i.e., the length of the DFT. To simplify the discussions, it is assumed that there are no overlapped frames in the neighboring blocks. Let $N_{block}$ be the number of blocks. It is further assumed $N_{frame}$ is equal to the product of $N_{block}$ and $N_{DFT}$.

The uPSP measurements of the $k$-th block are written as an $N_{node} \times N_{DFT}$ matrix of real numbers

$$Q_{uPSP}^{(k)} = [q_{uPSP,1}^{(k)} \quad q_{uPSP,2}^{(k)} \quad \cdots \quad q_{uPSP,s}^{(k)} \quad \cdots \quad q_{uPSP,N_{DFT}}^{(k)}] \tag{2}$$

where $Q_{uPSP}^{(k)} \in \mathbb{R}^{N_{node} \times N_{DFT}}$, $q_{uPSP,s}^{(k)} \in \mathbb{R}^{N_{node}}$, $k = 1, 2, \dots, N_{block}$, $s = 1, 2, \dots, N_{DFT}$. The output of the DFT of $Q_{uPSP}^{(k)}$, denoted as $\hat{Q}_{uPSP}^{(k)}$, is an $N_{node} \times N_{DFT}$ matrix of complex numbers

$$\hat{Q}_{uPSP}^{(k)} = \begin{bmatrix} \hat{q}_{uPSP,1}^{(k)} & \hat{q}_{uPSP,2}^{(k)} & \cdots & \hat{q}_{uPSP,m}^{(k)} & \cdots & \hat{q}_{uPSP,N_{DFT}}^{(k)} \end{bmatrix} \tag{3}$$

where $\hat{Q}_{uPSP}^{(k)} \in \mathbb{C}^{N_{node} \times N_{DFT}}$, $\hat{q}_{uPSP,m}^{(k)} \in \mathbb{C}^{N_{node}}$, $m = 1, 2, \dots, N_{DFT}$. $\mathbb{C}$ is the set of complex numbers. To simplify the discussions, a rectangular window is applied in the DFT.

The $m$-th column of the matrix $\hat{Q}_{uPSP}^{(k)}$, denoted as $\hat{q}_{uPSP,m}^{(k)}$ in Eq. (3), gives the frequency components of the original uPSP measurements in the $k$-th block at the frequency $f_m$, which is determined as

$$f_m = (m-1) \cdot f_{binWidth} \tag{4}$$

where $f_{binWidth}$ is the bin width of DFT, showing the frequency resolution. $f_{binWidth}$ is computed from the length of DFT, $N_{DFT}$, and the sample frequency of the uPSP measurements, $f_{sample}$, as shown below

$$f_{binWidth} = f_{sample} / N_{DFT} \tag{5}$$

The matrices $Q_{uPSP}^{(k)}$ and $\hat{Q}_{uPSP}^{(k)}$ describe the original uPSP measurements of the $k$-th block in the time and frequency domains, respectively. $\hat{Q}_{uPSP}^{(k)}$ is computed from $Q_{uPSP}^{(k)}$ with DFT and $Q_{uPSP}^{(k)}$ can be determined from $\hat{Q}_{uPSP}^{(k)}$ with Inverse DFT.

### B. Eigendecomposition of the Estimated CSD Matrix

In the second step of SPOD, the SPOD modes are determined through the eigendecomposition of the estimated CSD matrix at each frequency.

A matrix of the frequency components of the original uPSP measurements in all blocks on the selected grid nodes at the frequency $f_m$, denoted as $\hat{X}_{uPSP,m}$, is defined below

$$\hat{X}_{uPSP,m} = \begin{bmatrix} \hat{q}_{uPSP,m}^{(1)} & \hat{q}_{uPSP,m}^{(2)} & \cdots & \hat{q}_{uPSP,m}^{(k)} & \cdots & \hat{q}_{uPSP,m}^{(N_{block})} \end{bmatrix} \tag{6}$$

where $\hat{X}_{uPSP,m} \in \mathbb{C}^{N_{node} \times N_{block}}$ and the $k$-th column of $\hat{X}_{uPSP,m}$, $\hat{q}_{uPSP,m}^{(k)}$, is the $m$-th column of the matrix $\hat{Q}_{uPSP}^{(k)}$ in Eq. (3), $k = 1, 2, \dots, N_{block}$, $m = 1, 2, \dots, N_{DFT}$. The CSD matrix at the frequency $f_m$ is estimated from the matrix $\hat{X}_{uPSP,m}$ with Welch's method, as shown below

$$\hat{C}_m = (1/N_{block}) \cdot \hat{X}_{uPSP,m} \hat{X}_{uPSP,m}^* = (1/N_{block}) \cdot \sum_{k=1}^{N_{block}} \left[\hat{q}_{uPSP,m}^{(k)}\right] \left[\hat{q}_{uPSP,m}^{(k)}\right]^* \tag{7}$$

where $\hat{C}_m \in \mathbb{C}^{N_{node} \times N_{node}}$ and $(\cdot)^*$ denotes the conjugate transpose.

The SPOD modes at the frequency $f_m$ are determined as the eigenvectors of the estimated CSD matrix $\hat{C}_m$ and ranked in the descending order of the corresponding eigenvalues. Let $N_{mode}$ be the number of SPOD modes of the original uPSP measurements, we have

$$\hat{C}_m \hat{\Phi}_m = \hat{\Phi}_m \Lambda_m \tag{8}$$

where

$$\hat{\Phi}_m = \begin{bmatrix} \hat{\phi}_{m,1} & \hat{\phi}_{m,2} & \cdots & \hat{\phi}_{m,i} & \cdots & \hat{\phi}_{m,N_{mode}} \end{bmatrix} \tag{9}$$

$$\Lambda_m = \begin{bmatrix} \lambda_{m,1} & & & & & & \\ & \lambda_{m,2} & & & & & \\ & & \ddots & & & & \\ & & & \lambda_{m,i} & & & \\ & & & & \ddots & & \\ & & & & & \lambda_{m,N_{mode}} \end{bmatrix} \tag{10}$$

and

$$\lambda_{m,1} \geq \lambda_{m,2} \geq \cdots \geq \lambda_{m,i} \geq \cdots \geq \lambda_{m,N_{mode}} \geq 0 \tag{11}$$

In Eqs. (8)-(11), $\widehat{\Phi}_m \in \mathbb{C}^{N_{node} \times N_{mode}}$, $\hat{\phi}_{m,i} \in \mathbb{C}^{N_{node}}$, $\Lambda_m \in \mathbb{R}^{N_{mode} \times N_{mode}}$, $i = 1, 2, \ldots, N_{mode}$.

Note that $\hat{C}_m$ defined in Eq. (7) is a Hermitian matrix. Since the SPOD modes $\hat{\phi}_{m,i}$, $i = 1, 2, \ldots, N_{mode}$, are normalized, we have

$$\widehat{\Phi}_m^* \widehat{\Phi}_m = I_{N_{mode} \times N_{mode}} \tag{12}$$

where $I_{N_{mode} \times N_{mode}}$ is the identity matrix of the dimension $N_{mode} \times N_{mode}$. Eq. (12) shows the orthogonality of SPOD modes in space for a specific frequency.

### C. A Computational Shortcut

Since the number of selected grid nodes, $N_{node}$, is much larger than the number of blocks, $N_{block}$, a computational shortcut is taken to compute the eigenvectors and eigenvalues of the estimated CSD matrix $\hat{C}_m$ defined in Eq. (7).

First, an $N_{block} \times N_{block}$ Hermitian matrix is defined below from the matrix $\hat{X}_{uPSP,m}$

$$\widehat{M}_m = (1/N_{block}) \cdot \hat{X}_{uPSP,m}^* \hat{X}_{uPSP,m} \tag{13}$$

where $\widehat{M}_m \in \mathbb{C}^{N_{block} \times N_{block}}$. Then solve for the eigenvectors and eigenvalues of the matrix $\widehat{M}_m$, as shown below

$$\widehat{M}_m \widehat{\Psi}_m = \widehat{\Psi}_m \Lambda_m \tag{14}$$

where

$$\widehat{\Psi}_m = \begin{bmatrix} \hat{\psi}_{m,1} & \hat{\psi}_{m,2} & \cdots & \hat{\psi}_{m,i} & \cdots & \hat{\psi}_{m,N_{mode}} \end{bmatrix} \tag{15}$$

and $\widehat{\Psi}_m \in \mathbb{C}^{N_{block} \times N_{mode}}$, $\hat{\psi}_{m,i} \in \mathbb{C}^{N_{block}}$. Like Eq. (12),

$$\widehat{\Psi}_m^* \widehat{\Psi}_m = I_{N_{mode} \times N_{mode}} \tag{16}$$

Since $N_{node} \gg N_{block}$, the computation for the eigendecomposition of the matrix $\widehat{M}_m$ defined in Eq. (13) is much less than that for the eigendecomposition of the matrix $\hat{C}_m$ defined in Eq. (7). Finally, the eigenvectors of the estimated CSD matrix $\hat{C}_m$, i.e., the SPOD modes at the frequency $f_m$, are determined as

$$\widehat{\Phi}_m = \left(1/\sqrt{N_{block}}\right) \cdot \hat{X}_{uPSP,m} \widehat{\Psi}_m \Lambda_m^{-1/2} \tag{17}$$

### D. Inverse SPOD

The timeseries of the vortex shedding tones can be computed from the dominant SPOD modes of the original uPSP measurements with the Inverse SPOD algorithm, as shown below. The timeseries of the broadband signals are determined as the difference between the timeseries of the original uPSP measurements and the vortex shedding tones.

Equation (17) can be rewritten in the form below

$$\hat{X}_{uPSP,m} = \sqrt{N_{block}} \cdot \hat{\Phi}_m \Lambda_m^{1/2} \hat{\Psi}_m^* = \sqrt{N_{block}} \cdot \sum_{i=1}^{N_{mode}} \lambda_{m,i}^{1/2} \hat{\phi}_{m,i} \hat{\psi}_{m,i}^* \tag{18}$$

Let $N_{mode,VS}$ be number of dominant SPOD modes of the vortex shedding tones. Note that $N_{mode,VS} < N_{mode}$. Define a matrix of vortex shedding tones in the frequency domain

$$\hat{X}_{VS,m} = \sqrt{N_{block}} \cdot \sum_{i=1}^{N_{mode,VS}} \lambda_{m,i}^{1/2} \hat{\phi}_{m,i} \hat{\psi}_{m,i}^* \tag{19}$$

The matrix $\hat{X}_{VS,m}$ has the same size as the matrix $\hat{X}_{uPSP,m}$ and is rewritten in the same form of Eq. (6), as shown below

$$\hat{X}_{VS,m} = \begin{bmatrix} \hat{q}_{VS,m}^{(1)} & \hat{q}_{VS,m}^{(2)} & \cdots & \hat{q}_{VS,m}^{(k)} & \cdots & \hat{q}_{VS,m}^{(N_{block})} \end{bmatrix} \tag{20}$$

where $\hat{X}_{VS,m} \in \mathbb{C}^{N_{node} \times N_{block}}$, $\hat{q}_{VS,m}^{(k)} \in \mathbb{C}^{N_{node}}$, $m = 1, 2, \ldots, N_{DFT}$, and $k = 1, 2, \ldots, N_{block}$. Since the matrix $\hat{X}_{VS,m}$ includes the dominant SPOD modes of the vortex shedding tones, it can be viewed as an approximation of the matrix $\hat{X}_{uPSP,m}$. Considering the *k*-th column of the matrices $\hat{X}_{VS,m}$ and $\hat{X}_{uPSP,m}$, the complex vector $\hat{q}_{VS,m}^{(k)}$ can be viewed as an approximation of the complex vector $\hat{q}_{uPSP,m}^{(k)}$. Each member of the complex vector $\hat{q}_{VS,m}^{(k)}$ describes a sinusoidal signal oscillating at the frequency $f_m$, where $m = 1, 2, \ldots, N_{DFT}$, in the frequency domain.

Like in Eq. (3), a matrix of complex numbers, describing the vortex shedding tones of the *k*-th block in the frequency domain, can be built from $\hat{q}_{VS,m}^{(k)}$, where $m = 1, 2, \ldots, N_{DFT}$, as shown below

$$\hat{Q}_{VS}^{(k)} = \begin{bmatrix} \hat{q}_{VS,1}^{(k)} & \hat{q}_{VS,2}^{(k)} & \cdots & \hat{q}_{VS,m}^{(k)} & \cdots & \hat{q}_{VS,N_{DFT}}^{(k)} \end{bmatrix} \tag{21}$$

where $\hat{Q}_{VS}^{(k)} \in \mathbb{C}^{N_{node} \times N_{DFT}}$. A row of the matrix $\hat{Q}_{VS}^{(k)}$ can be viewed as the DFT of a timeseries of the vortex shedding tones of the *k*-th block on a selected grid node. The timeseries can be determined from the row of $\hat{Q}_{VS}^{(k)}$ with Inverse DFT. Like in Eq. (2), the timeseries of the vortex shedding tones of the *k*-th block on the selected grid nodes are written in a matrix of real numbers

$$Q_{VS}^{(k)} = \begin{bmatrix} q_{VS,1}^{(k)} & q_{VS,2}^{(k)} & \cdots & q_{VS,s}^{(k)} & \cdots & q_{VS,N_{DFT}}^{(k)} \end{bmatrix} \tag{22}$$

where $Q_{VS}^{(k)} \in \mathbb{R}^{N_{node} \times N_{DFT}}$, $k = 1, 2, \ldots, N_{block}$, $s = 1, 2, \ldots, N_{DFT}$.

The matrix of the full timeseries of the vortex shedding tones on the selected grid nodes, denoted as $Q_{VS}$, is built from $Q_{VS}^{(k)}$ as following

$$Q_{VS} = \begin{bmatrix} Q_{VS}^{(1)} & Q_{VS}^{(2)} & \cdots & Q_{VS}^{(k)} & \cdots & Q_{VS}^{(N_{block})} \end{bmatrix} \tag{23}$$

where $Q_{VS} \in \mathbb{R}^{N_{node} \times N_{frame}}$, $k = 1, 2, \ldots, N_{block}$. The matrix of the full timeseries of the broadband signals, denoted as $Q_{BB}$, is determined as

$$Q_{BB} = Q_{uPSP} - Q_{VS} \tag{24}$$

where $Q_{BB} \in \mathbb{R}^{N_{node} \times N_{frame}}$.

## III. SPOD of uPSP Measurements of a SLS Force & Moment Test

In this section, the SPOD algorithm is used on the original uPSP measurements in the tests of a Mach sweep run of a SLS Force & Moment Test. A set of grid nodes are selected on the center body of the model, the parameters of SPOD are discussed and the outputs of SPOD of the original uPSP measurements on the selected grid nodes are presented. The freestream Mach numbers of the tests are 0.90 through 1.40 in increments of 0.10. The angle of attack and the angle of sideslip are both zero degrees.

### A. Selected Grid Nodes

To investigate the characteristics of the vortex shedding tones, a set of 78,932 grid nodes are selected in the neighboring areas of the forward attachments of the left and right SRBs on the surface of the center body of the scale model. Figure 3 shows the grid nodes of the center body of the scale model, illustrated as black dots, in the plane of the X-coordinate and azimuth of the nodes. The selected grid nodes are illustrated as red dots. Note that the X axis of the SLS coordinate system is defined on the center line of the center body of the launch vehicle, pointing in the downstream direction. The azimuth angles of the center lines of the left and right SRBs are 90° and 270°, respectively. Figure 3 also shows the forward attachments of the left and right SRBs as well as the areas of camera view blockage by the SRBs, where the uPSP measurements are unavailable.

The timeseries of average pressures were generated on a set of patches with the datasets of separated vortex shedding tones and broadband signals for the structural dynamics analysis of the SLS launch vehicle. As shown in Fig. 3, 288 patches, illustrated as blue boxes, are arranged in 12 columns. The columns in the group of the left SRB are labeled as Columns A, B, C, D, E and F. The columns in the group of the right SRB are labeled as Columns G, H, I, J, K and L. In each column there are 24 patches, whose ranges of the azimuth angle are the same.

A patch of Column D, located at the downstream side of the forward attachment of the left SRB, is selected as a reference. The selected grid nodes in the reference patch are illustrated as green dots in Fig. 3. In Section IV, we will present the timeseries of average pressures and the corresponding Power Spectral Densities (PSDs) generated from the datasets of original uPSP measurements, vortex shedding tones and broadband signals on the selected grid nodes in the reference patch.

### B. Parameters of SPOD of uPSP Measurements

Table 1 shows the parameters of SPOD of the uPSP measurements in the tests of the Mach sweep run of the SLS Force & Moment Test. As shown in the table, the timeseries of uPSP measurements on the 78,932 selected grid nodes are used to generate the SPOD outputs. The 49,152 frames of uPSP measurements are partitioned into 12 non-overlapping blocks and there are 4,096 frames in each block.

The number of SPOD modes, $N_{mode}$, is determined by the rank of matrix $\hat{X}_{uPSP,m}$ defined in Eq. (6), which is limited by the number of selected grid nodes, $N_{node}$, and the number of blocks, $N_{block}$. Since $N_{node} \gg N_{block}$, $N_{mode} = N_{block} = 12$, as shown in Table 1.

Note that a rectangular window is applied in the DFT of the uPSP measurements in each block and a uniform weighting function is used to process the data. The sample frequency $f_{sample} = 10{,}000\ Hz$. For the SPOD outputs presented in this paper, the frequency resolution, i.e., the bin width of DFT, $f_{binWidth} = 10{,}000\ Hz/4{,}096 = 2.44\ Hz$.

**Table 1. Parameters of SPOD of the uPSP measurements in the tests of the Mach sweep run of the SLS Force & Moment Test**

| Parameter | Value |
|---|---|
| Spectral Type | one-sided (real-valued signal) |
| Number of Selected Grid Nodes, $N_{node}$ | 78,932 |
| Number of Total Frames, $N_{frame}$ | 49,152 |
| Number of Frames per Block, $N_{DFT}$ | 4,096 |
| Number of Blocks, $N_{block}$ | 12 |
| Number of SPOD Modes, $N_{mode}$ | 12 |
| Windowing Function (time) | rectangular window |
| Weighting Function (space) | uniform |
| Sample Frequency (Hz), $f_{sample}$ | 10,000 |
| Frequency Resolution (Hz), $f_{binWidth}$ | 2.44 |

### C. Energy of SPOD Modes of uPSP Measurements

As an example, Fig. 4 shows the energy (unit: $psi^2$, in logarithmic scale) of the SPOD modes of the original uPSP measurements on the selected grid nodes at Mach number 1.20, as the function of frequency (unit: Hz, in linear scale), in a frequency band of interest. The energies of the 1st and 2nd SPOD modes are illustrated in red and blue lines, respectively. The frequencies of the vortex shedding tones generated by the forward attachments of the left and right SRBs are different. As shown in Fig. 4, the 1st harmonic frequencies of the vortex shedding tones of the left and right SRBs are illustrated in green and magenta vertical dash lines respectively, and the 2nd harmonic frequencies are illustrated in green and magenta vertical dash-dotted lines respectively. The energy of the 1st SPOD mode is at its local peaks at the 1st and 2nd harmonic frequencies of the vortex shedding tones of the left and right SRBs.

Figure 5 shows the percentage of the energy of the 1st and 2nd SPOD modes (in red and blue lines, respectively) as well as the sum of the 1st and 2nd modes (in black line) in the energy of all 12 SPOD modes for the same test condition as Fig. 4 as the function of frequency (unit: Hz, in linear scale), in the same frequency band of interest as Fig. 4. Like in Fig. 4, the 1st harmonic frequencies of the vortex shedding tones of the left and right SRBs are illustrated in green and magenta vertical dash lines respectively, and the 2nd harmonic frequencies are illustrated in green and magenta dash-dotted lines respectively. The 1st SPOD mode occupies more than 94% of the energy of all SPOD modes at the 1st harmonic frequencies and more than 45% of the energy of all SPOD modes at the 2nd harmonic frequencies. Computations show the 1st and 2nd SPOD modes occupy 75.7% in total of the energy of all SPOD modes in the interested frequency band.

Table 2 shows the percentage of the energy of the 1st and 2nd SPOD modes in the energy of all 12 SPOD modes of the uPSP measurements at the 1st harmonic frequencies of the vortex shedding tones of the left and right SRBs as well as in the interested frequency band. As shown in the table, the 1st and 2nd SPOD modes occupy more than 94% in total of the energy of all SPOD modes at the 1st harmonic frequencies and more than 66% in total of the energy of all SPOD modes in the interested frequency band. Therefore, the 1st and 2nd SPOD modes of the original uPSP measurements are dominant modes of the vortex shedding tones of the left and right SRBs.

**Table 2. Percentage of the energy of the 1st and 2nd SPOD modes in the energy of all SPOD modes of the original uPSP measurements in the Mach sweep run of the SLS Force & Moment Test**

| **Mach Number** | | 0.90 | 1.00 | 1.10 | 1.20 | 1.30 | 1.40 |
|---|---|---|---|---|---|---|---|
| **At 1st Harmonic Frequency of Vortex Shedding Tone of Left SRB** | 1st Mode | 89.6% | 95.6% | 86.5% | 95.7% | 97.3% | 91.8% |
| | 2nd Mode | 8.6% | 3.5% | 12.5% | 3.5% | 1.2% | 4.5% |
| | Sum | 98.2% | 99.1% | 99.0% | 99.2% | 98.5% | 96.3% |
| **At 1st Harmonic Frequency of Vortex Shedding Tone of Right SRB** | 1st Mode | 91.4% | 94.8% | 82.9% | 94.2% | 93.2% | 75.9% |
| | 2nd Mode | 4.9% | 3.7% | 15.3% | 4.4% | 2.0% | 18.6% |
| | Sum | 96.3% | 98.5% | 98.2% | 98.6% | 95.2% | 94.5% |
| **In Interested Frequency Band** | 1st Mode | 50.4% | 60.9% | 55.0% | 62.0% | 63.2% | 56.1% |
| | 2nd Mode | 16.3% | 14.8% | 19.3% | 13.7% | 11.5% | 17.5% |
| | Sum | 66.7% | 75.7% | 74.3% | 75.7% | 74.7% | 73.6% |

## IV. Separation of Vortex Shedding Tones and Broadband Signals

From the dominant SPOD modes of the original uPSP measurements, the dataset of timeseries of the vortex shedding tones was generated with Eq. (19) in Section II, where the number of dominant modes, $N_{mode,VS}$, was set to two. The dataset of timeseries of the broadband signals was generated with Eq. (24). As examples, the SPOD outputs, PSDs and spectrograms are generated from the datasets of timeseries of the vortex shedding tones and broadband signals as well as the original uPSP measurements and the effectiveness of the separation of vortex shedding tones and broadband signals is demonstrated.

The SPOD algorithm is used again to process the datasets of timeseries of the vortex shedding tones and broadband signals. Figures 6(a) and 6(b) show the energy (unit: $psi^2$, in logarithmic scale) of SPOD modes of the two datasets as the function of frequency (unit: Hz, in linear scale), in the same frequency band of interest as Fig. 4. The parameters of SPOD are the same as those in Table 1. Comparing Figs. 4 and 6(a), it is observed that there are only

two SPOD modes in the dataset of the vortex shedding tones, which are equivalent to the 1st and 2nd SPOD modes of the original uPSP measurements. As expected, there are no dominant modes of vortex shedding tones in the outputs of SPOD of the dataset of the broadband signals, as shown in Fig. 6(b).

The timeseries of average pressures are generated from three datasets of original uPSP measurements, vortex shedding tones and broadband signals on 288 patches, as illustrated in Fig. 3, for the structural dynamics analysis of the SLS launch vehicle. A patch of Column D is selected as a reference. Figures 7(a1), 7(a2) and 7(a3) show the timeseries of average pressures (unit: psi, in linear scale), generated from three datasets of original uPSP measurements, vortex shedding tones and broadband signals, respectively, on the 260 selected grid nodes in the reference patch. Figures 7(b1), 7(b2) and 7(b3) show the corresponding PSDs (unit: $psi^2$/Hz, in logarithmic scale) as the function of frequency (unit: Hz, in linear scale), in the same interested frequency band as Fig. 4. The peaks of PSD at the 1st and 2nd harmonic frequencies of vortex shedding tone of the left SRB can be observed in Figs. 7(b1) and 7(b2) and there are no peaks at the same frequencies shown in Fig. 7(b3).

Figure 8 shows the spectrograms of average pressures on the patches in Columns A, B, C, D, E and F in the group of the left SRB. In each spectrogram, the horizontal axis shows the X-coordinate of the patches, and the vertical axis shows the frequency (unit: Hz, in linear scale), in the same frequency band of interest as Fig. 4. The spectrograms, generated from three datasets of original uPSP measurements, vortex shedding tones and broadband signals, are shown in the 1st, 2nd and 3rd columns in Fig. 8, respectively, plotted in the same colormap. The 1st and 2nd harmonics of vortex shedding tones can be observed in the spectrograms generated from the datasets of original uPSP measurements and vortex shedding tones on the patches downstream of the forward attachment of the left SRB. There are no vortex shedding tones observed in the spectrograms generated from the dataset of broadband signals. It is observed the spectrograms of average pressures on the six columns of patches in the group of the left SRB are symmetric to the half plane at azimuth 90°. As expected, the 1st and 2nd harmonics of vortex shedding tones are stronger in the spectrograms of average pressures when the azimuth angles of the patches are closer to 90°.

Figure 9 shows the spectrograms of average pressures on the patches in Columns G, H, I, J, K and L in the group of the right SRB, plotted in the same colormap as Fig. 8 and in the same interested frequency band as Fig. 4. Similar characteristics as seen in Fig. 8, e.g., no vortex shedding tones in the spectrograms generated from the dataset of broadband signals, symmetry of spectrograms of average pressures to the half plane at azimuth 270°, etc., can be observed in Fig. 9. Comparing Figs. 8 and 9, the difference in the frequencies of vortex shedding tones of the left and right SRBs are apparent.

The outputs shown in Figs. 6-9 demonstrate the original uPSP measurements are effectively separated into two parts — vortex shedding tones and broadband signals.

## V. Visualization of SPOD Modes of Vortex Shedding Tones

In this section, we present characteristics of the vortex shedding tones, generated by the forward attachments of the left and right SRBs, through visualization of SPOD modes in the frequency and time domains, respectively. As examples, the SPOD modes generated from the dataset of the vortex shedding tones, which is separated from the original uPSP measurements on the selected grid nodes in the supersonic test at Mach number 1.20 of the SLS Force & Moment Test, are presented and discussed.

### A. Visualization of SPOD Modes of Vortex Shedding Tones in Frequency Domain

Figure 10 shows the energy (unit: $psi^2$, in logarithmic scale) of the two SPOD modes of the dataset of vortex shedding tones, as the function of frequency (unit: Hz, in linear scale), in the same frequency band of interest as Fig. 4. Compared to Fig. 6(a), Fig. 10 focuses on a smaller frequency band. The energy of the 1st SPOD mode is at its local peaks at the 1st harmonic frequencies of the vortex shedding tones of the left and right SRBs, which are illustrated in green and magenta vertical dash lines, respectively. As shown in Fig. 10, a reference frequency, illustrated in a black vertical dash line, is selected, at which the energy of the 1st SPOD mode is at its local valley and the energy of the 2nd SPOD mode is at its local peak.

Figures 11 and 12 show the magnitudes and phases of the 1st and 2nd SPOD modes at the 1st harmonic frequency of the vortex shedding tone of the left SRB and the 1st harmonic frequency of the vortex shedding tone of the right SRB, respectively, plotted on the plane of the X-coordinate and azimuth of the nodes. Note that the azimuth ranges from 0° to 360° in Figs. 11 and 12. The SPOD modes are nondimensional, so are their magnitudes. The magnitudes are plotted in the logarithmic scale with the same colormap. The phase of the SPOD modes ranges from -180° to +180°.

The grid nodes with the phase close to -180° are plotted in blue and the grid nodes with the phase close to +180° are plotted in yellow.

In Fig. 11, at the 1st harmonic frequency of the vortex shedding tone of the left SRB, larger magnitude of the 1st SPOD mode is observed on the selected grid nodes which are located downstream of the forward attachment of the left SRB and whose azimuth angles are in the range from 30° to 150°, and larger magnitude of the 2nd SPOD mode is observed on the selected grid nodes which are located downstream of the forward attachment of the right SRB and whose azimuth angles are in the range from 210° to 330°. Figure 11 demonstrates an important characteristic of SPOD — the orthogonality of modes in space at a specific frequency makes SPOD an effective tool to detect and identify less energetic modes, which are shadowed by dominant modes in DMD. As shown in Fig. 11, at the 1st harmonic frequency of the vortex shedding tone of the left SRB, the vortex shedding tone generated by the forward attachment of the left SRB is dominant, so it is detected and identified as the 1st SPOD mode. Once the 1st SPOD mode is removed, the vortex shedding tone generated by the forward attachment of the right SRB is dominant in the residual and is detected and identified as the 2nd SPOD mode.

Similarly, in Fig. 12, at the 1st harmonic frequency of the vortex shedding tone of the right SRB, the vortex shedding tone generated by the forward attachment of the right SRB is dominant, so it is detected and identified as the 1st SPOD mode. Then the vortex shedding tone generated by the forward attachment of the left SRB is detected and identified as the 2nd SPOD mode.

Figures 11 and 12 show that the 1st SPOD modes at frequencies lower than the reference frequency and the 2nd SPOD modes at frequencies higher than the reference frequency correspond to the vortex shedding tones generated by the forward attachment of the left SRB. Similarly, the 2nd SPOD modes at frequencies lower than the reference frequency and the 1st SPOD modes at frequencies higher than the reference frequency correspond to the vortex shedding tones generated by the forward attachment of the right SRB.

### B. Visualization of SPOD Modes of Vortex Shedding Tones in Time Domain

Figures 13 and 14 show the 1st SPOD mode of the vortex shedding tones on the selected grid nodes at the 1st harmonic frequencies of the vortex shedding tones of the left and right SRBs, respectively, at phases 0° through 345° in increments of 15°, in the time domain and plotted on the plane of the X-coordinate and azimuth of the nodes. The azimuth ranges from 0° to 180° in Fig. 13 and from 180° to 360° in Fig. 14. As shown in Figs. 13 and 14, the peaks of the vortex shedding tones, originated from the forward attachments of the left and right SRBs, move in the downstream direction. The red arrows in the subplots of Figs. 13 and 14 at phases of 0°, 45°, 90°, 135° and 180° point to the grid nodes symmetric to the half planes at azimuth of 90° and 270°, respectively. It is observed the 1st SPOD mode at the 1st harmonic frequency of the vortex shedding tone is out of phase by 180° on the grid nodes highlighted by the red arrows.

Figures 15 and 16 show the 1st SPOD mode of the vortex shedding tones on the selected grid nodes at the 2nd harmonic frequencies of vortex shedding tones of the left and right SRBs, respectively, at phases 0° through 345° in increments of 15° in the time domain, plotted on the plane of the X-coordinate and azimuth of the nodes. The azimuth ranges from 0° to 180° in Fig. 15 and from 180° to 360° in Fig. 16. Compared to the wavelengths of the vortex shedding tones at the 1st harmonic frequencies, it is observed the wavelengths of the vortex shedding tones at the 2nd harmonic frequencies decrease by half. The red arrows in the subplots of Figs. 15 and 16 at phases of 0°, 45°, 90°, 135° and 180° point to the grid nodes symmetric to the half planes at azimuth of 90° and 270°, respectively. It is interesting to note that the 1st SPOD mode at the 2nd harmonic frequency of the vortex shedding tone has the same phase on the grid nodes highlighted by the red arrows.

## VI. Conclusions

In this paper, the outputs of SPOD of uPSP measurements, which were collected during an SLS Force & Moment Test at NASA Ames Research Center in April 2025, are presented. Vortex shedding tones, generated by the forward attachments of the left and right SRBs of the SLS launch vehicle, were consistently observed in the uPSP measurements. A dataset of timeseries of the vortex shedding tones is generated from the dominant SPOD modes of the original uPSP measurements with Inverse SPOD and another dataset of timeseries of the broadband signals is generated as the difference of the datasets of the original uPSP measurements and vortex shedding tones. The effectiveness of the separation of the vortex shedding tones and broadband signals is demonstrated by the comparison of the SPOD outputs, PSDs and spectrograms generated from the timeseries of the separated vortex shedding tones and broadband signals as well as the original uPSP measurements.

The characteristics of the vortex shedding tones are also presented in this paper. It is demonstrated, by taking advantage of the well-known property that the measurements of the uPSP have much higher spatial resolution compared to those of the conventional pressure transducers, the visualization of SPOD modes provides an effective tool in the detection and identification of complicated aerodynamic and aeroacoustic phenomena, possibly generated by different physical processes.

In the future, the methodology described in this paper will be used to process the SLS simulation results so that their separated vortex shedding tones and broadband signals can be compared with the corresponding parts of the uPSP measurements.

## Acknowledgment

The research work in this paper was funded by the NASA Aerosciences Evaluation and Test Capabilities Portfolio Office of the Aeronautics Research Mission Directorate. The authors would like to thank Bruce LaVerde of NASA Marshall Space Flight Center and Christopher Henze of NASA Advanced Supercomputing Division at Ames Research Center for their education and advice. The authors also would like to thank Avraham Gileadi for his expertise to support the SLS Force & Moment Test. Thanks to: James Bell, Paul Bremner, Lawrence Hand, Andrew Meade, Blair Mclachlan, Rabindra Mehta, Jayanta Panda, James Ross and Nathanial Smith for their education and advice on the fluid mechanics and signal processing. Thanks to: Ryan Connelly, Oleg Goushcha, Patrick Heaney, Jaffar Iqbal, Seth Kelly, Alan Landman, David Piatak, Jeremy Pinier, James Ramey, Martin Sekula, Patrick Shea, Francesco Soranna, Thomas Steva, Craig Streett, Cory Wilbanks and Timothy Wray for their education and advice on the SLS. Thanks to: Stephen Cotton, David Ellsworth, Nina McCurdy, Patrick Moran, Bron Nelson and Timothy Sandstrom for their education and advice on the software development and parallel processing. Thanks to: Michael Barad, Derek Dalle, Jeffrey Housman and Gerrit-Daniel Stich for their expertise and advice on the SLS modeling and simulations. Finally, thanks to: Max Amaya, Jennifer Baerny, Colin Davis, Maureen Delgado, Jennifer Everett, Ross Flach, Theodore Garbeff, Samuel Morice, James Prunty, Hannah Spooner, Tim Steiger, Mike Treece, Thomas Volden, Michael Weiss and the rest of the Ames UPWT staff for their assistance in executing the wind tunnel test. The authors also thank the SLS team for the use of the scale model and the UPWT instrumentation and operation team of NASA Ames Research Center for the support of the SLS Force & Moment Test.

## References

[1] Innovative Scientific Solutions, Inc., Porous, Fast-Response Pressure Sensitive Paint Data Sheet. https://innssi.com/wp-content/uploads/Pressure_Sensitive_Paint/Porous_Fast_PSP/Documentation/Porous-Fast-Response-PSP-FP-XXX-Data-Sheet.pdf. Accessed: 13 May 2025.

[2] Li, J., Lash, E. L., Roozeboom, N. H., Garbeff, T. J., Henze, C. E., Murakami, D. D., Smith, N. T., Baerny, J. K., Hand, L. A., Shaw-Lecerf, M. A., Stremel, P. M., and Tang, L. Z., "Dynamic Mode Decomposition of Unsteady Pressure-Sensitive Paint Measurements for the NASA Unitary Plan Wind Tunnel Tests", AIAA Paper 2022-0141, AIAA SciTech Forum, San Diego, CA & Virtual, January 2022.

[3] Li, J., Roozeboom, N. H., Lash, E. L., Shaw-Lecerf, M. A., Baerny, J. K., Garbeff, T. J., Hand, L. A., Henze, C. E., Murakami, D. D., and Smith, N. T., "Aeroacoustic Analysis using Dynamic Mode Decomposition of Unsteady Pressure-Sensitive Paint Measurements", AIAA Paper 2024-0882, AIAA SciTech Forum, Orlando, FL, January 2024.

[4] Towne, A., Schmidt, O. T. and Colonius, T., "Spectral Proper Orthogonal Decomposition and Its Relationship to Dynamic Mode Decomposition and Resolvent Analysis", *Journal of Fluid Mechanics*, Vol. 847, pp. 821-867, 2018.

[5] Schmidt, O. T. and Colonius, T., "Guide to Spectral Proper Orthogonal Decomposition", *AIAA Journal*, Vol. 58, No. 3, pp. 1023-1033, 2020.

[6] Nekkanti, A. and Schmidt, O. T., Frequency-Time Analysis, Low-Rank Reconstruction and Denoising of Turbulent Flows using SPOD", *Journal of Fluid Mechanics*, Vol. 926, A26, 2021.

[7] Li, J., Lash, E. L., Lyons, K. R., Roozeboom, N. H., Shaw-Lecerf, M. A., Murakami, D. D., and Califano, N. W. W., "Spectral Proper Orthogonal Decomposition of Unsteady Pressure-Sensitive Paint Measurements in Recent NASA Ames Wind Tunnel Test", AIAA Paper 2025-0234, AIAA SciTech Forum, Orlando, FL, January 2025.

[8] Soranna, F., Heaney, P. S., Sekula, M. K., Piatak, D. J., and Ramey, J. M., "Space Launch System Unsteady Forces Developed from Unsteady-Pressure-Sensitive-Paint-based Corcos Model Parameters", *Journal of Spacecraft and Rockets*, Vol. 61, No. 2, March-April 2024.

[9] Schuster, D. M., Panda, J., Ross, J. C., Roozeboom, N. H., Burnside, N., Ngo, C. L., Kumagai, H., Sellers, M. E., Powell, J. M., Sekula, M. K., and Piatak, D. J., "Investigation of Unsteady Pressure-Sensitive Paint (uPSP) and a Dynamic Loads Balance to Predict Launch Vehicle Buffet Environments", NASA Engineering and Safety Center Report TI-14-00962, 2016.

[10] Roozeboom, N. H., Diosady, L. T., Murman, S. M., Burnside, N. J., Panda, J., and Ross, J. C., "Unsteady PSP Measurements on a Flat Plate Subject to Vortex Shedding from a Rectangular Prism", AIAA Paper 2016-2017, 54th AIAA Aerospace Sciences Meeting, San Diego, CA, January 2016.

[11] Panda, J., "Experimental Verification of Buffet Calculation Procedure Using Unsteady Pressure-Sensitive Paint", *Journal of Aircraft*, Vol.54, No. 5, 2017, pp. 1791-1801.

[12] Sellers, M. E., Nelson, M. A., Roozeboom, N. H., and Burnside, N. J., "Evaluation of Unsteady Pressure Sensitive Paint Measurement Technique for Space Launch Vehicle Buffet Determination", AIAA Paper 2017-1402, 55th AIAA Aerospace Sciences Meeting, Grapevine, TX, January 2017.

[13] Roozeboom, N. H., Ngo, C. L., Powell, J. M., Murakami, D. D., Ross, J. C., Murman, S. M., and Baerny, J. K., "Data Processing Methods for Unsteady Pressure-Sensitive Paint Application", AIAA 2018-1031, 56th AIAA Aerospace Sciences Meeting, Kissimmee, Florida, January 2018.

[14] Panda, J., Roozeboom, N.H., and Ross, J. C., "Wavenumber-Frequency Spectra on a Launch Vehicle Model Measured via Unsteady Pressure-Sensitive Paint", *AIAA Journal*, Vol. 57, No. 5, 2019, pp. 1801-1817.

[15] Roozeboom, N. H., Powell, J. M., Baerny, J. K., Murakami, D. D., Ngo, C. L., Garbeff, T. J., Ross, J. C., and Flach, R. L., "Development of Unsteady Pressure-Sensitive Paint Application on NASA Space Launch System", AIAA Paper 2019-3502, AIAA Aviation Forum, Dallas, TX, June 2019.

[16] Roozeboom, N. H., Murakami, D. D., Li, J., Powell, J. M., Baerny, J. K., Stremel, P. M., Volden, T. R., Flach, R. L., Douthitt, A. N., Steva, T. B., Ross, J. C., and Bell, J. H., "Recent Developments in NASA's Unsteady Pressure-Sensitive Paint Capability", AIAA Paper 2020-0516, AIAA SciTech Forum, Orlando, FL, January 2020.

[17] Roozeboom, N., Murakami, D., Li, J., Shaw-Lecerf, M., Lash, E.L, Califano, N., Stremel, P., Lyons, K., Baerny, J., Barreras, C., Ortega, J., Kato, K., Hand, L. and McLachlan, B., "NASA's Unsteady Pressure-Sensitive Paint Research and Operational Capability Developments", AIAA Paper 2023-0636, AIAA SciTech Forum, National Harbor, MD & Virtual, January 2023.

[18] Lash, E. L, Roozeboom, N. H., Murakami, D. D., Shaw-Lecerf, M. A., Li, J., Califano, N. W., Lyons, K. R., Stremel, P. M., Baerny, J., Barreras, C. E., Ortega, J. and Hand, L. A., "NASA's Unsteady Pressure-Sensitive Paint Phase I Development Overview", AIAA Paper 2024-0880, AIAA SciTech Forum, Orlando, FL, January 2024.

[19] Lash, E. L, Murakami, D. D., Shaw-Lecerf, M. A., Lyons, K. R., Li, J., Califano, N., Crowe, E. D. and Roozeboom, N. H., "uPSP Launch Vehicle Demonstration Test at NASA Ames Research Center", AIAA Paper 2025-0232, AIAA SciTech Forum, Orlando, FL, January 2025.

[20] Powell, J. M., Murman, S. M., Ngo, C. L., Roozeboom, N. H., Murakami, D. D., Baerny, J. K., and Li, J., "Development of Unsteady-PSP Data Processing and Analysis Tools for the NASA Ames Unitary 11ft Wind Tunnel", AIAA Paper 2020-0292, AIAA SciTech Forum, Orlando, FL, January 2020.

[21] Shaw-Lecerf, M. A., Lash, E. L, Lyons, K. R., Murakami, D. D., Roozeboom, N. H., Li, J., and Califano, N., "Spatiotemporal Analysis of High-Resolution Pressure-Sensitive Paint Measurements on a Launch Vehicle Wind Tunnel Model", AIAA Paper 2025-0235, AIAA SciTech Forum, Orlando, FL, January 2025.

[22] MATLAB Documentation: spod. https://www.mathworks.com/matlabcentral/fileexchange/65683-spectral-proper-orthogonal-decomposition-spod. Accessed: 26 March 2024.

[23] Mengaldo, G. and Maulik, R., "PySPOD: A Python package for Spectral Proper Orthogonal Decomposition (SPOD)", *Journal of Open Source Software*, 6(60), 2862, 2021.



**Figure 1**. Scale model of the SLS Block 1 crew vehicle with uPSP in the 11-by 11-ft transonic wind tunnel at NASA Ames Research Center during a Force & Moment Test in April 2025.

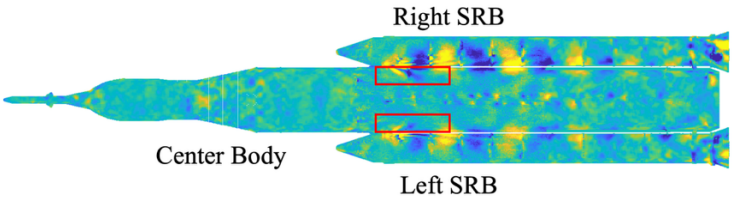


**Figure 2.** DMD mode of the uPSP measurements at the frequency of the vortex shedding tone in the supersonic test at Mach number 1.20. The two red boxes illustrate the areas of selected grid nodes.

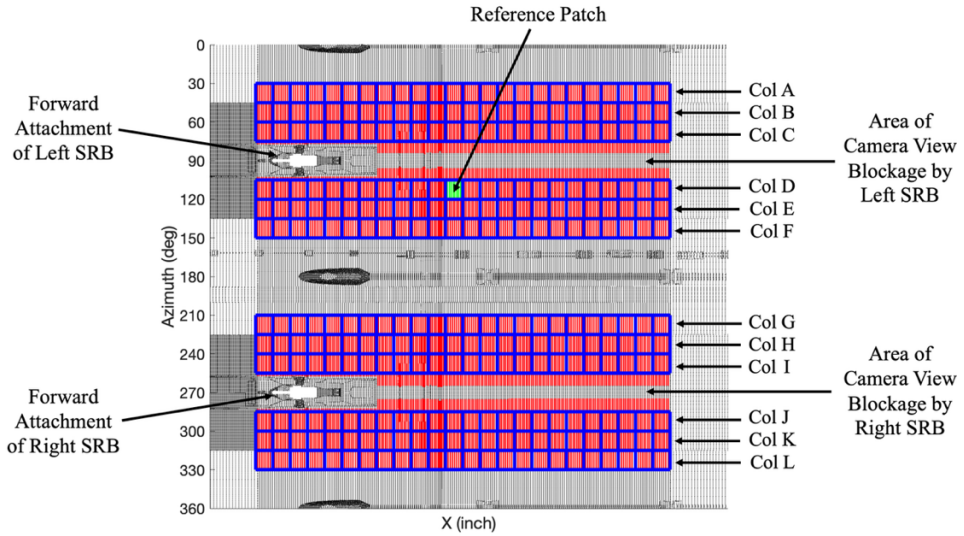


**Figure 3.** Grid nodes of the SLS center body, plotted on the plane of the X-coordinate and azimuth of the nodes. The selected grid nodes are illustrated as red dots. A set of 288 patches, illustrated as blue boxes, are arranged in 12 columns. One of the patches is selected as a reference. The selected grid nodes in the reference patch are illustrated as green dots.

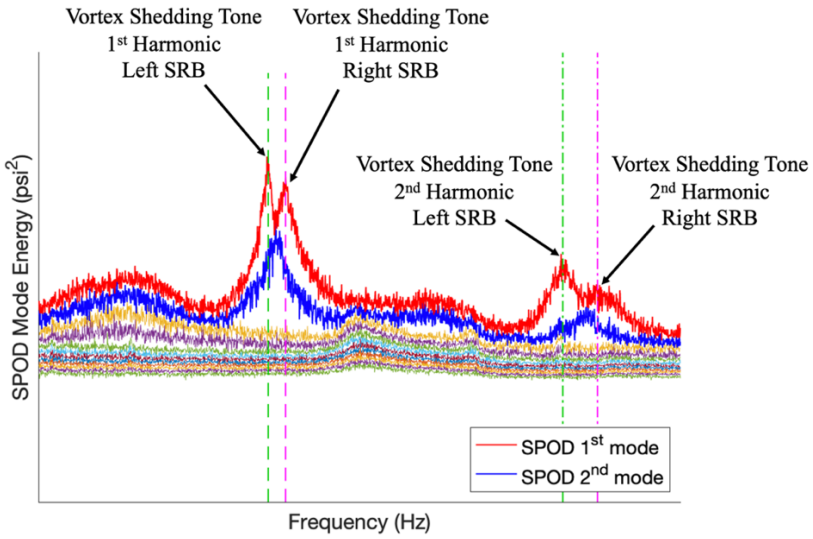


**Figure 4.** Energy of SPOD modes of the original uPSP measurements on the selected grid nodes in the supersonic test at Mach number 1.20 of the SLS Force & Moment Test as the function of frequency, in the interested frequency band. The 1st harmonic frequencies of the vortex shedding tones of the left and right SRBs are illustrated in green and magenta vertical dash lines respectively, and the 2nd harmonic frequencies are illustrated in green and magenta vertical dash-dotted lines respectively.

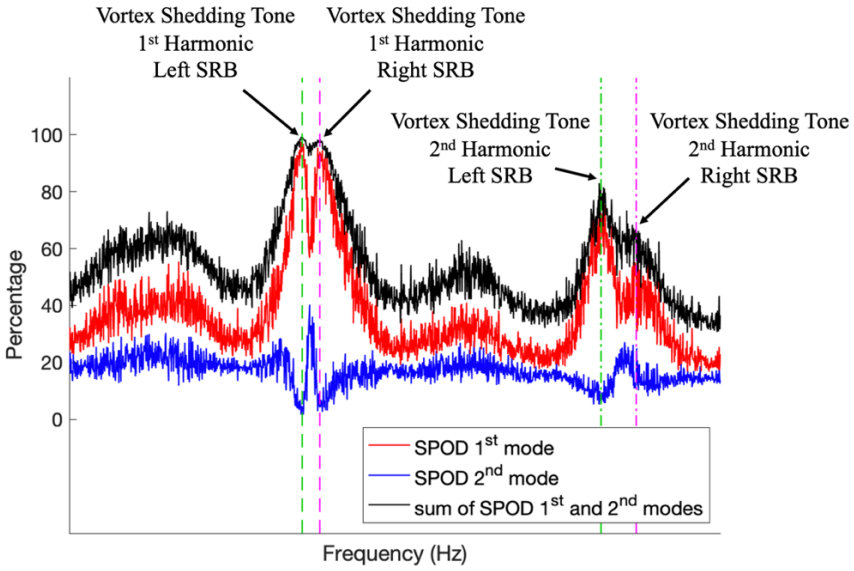


**Figure 5.** Percentage of the energy of the 1st and 2nd SPOD modes as well as the sum of the 1st and 2nd modes in the energy of all SPOD modes of the original uPSP measurements on the selected grid nodes in the supersonic test at Mach number 1.20 of the SLS Force & Moment Test as the function of frequency, in the interested frequency band. The 1st harmonic frequencies of the vortex shedding tones of the left and right SRBs are illustrated in green and magenta vertical dash lines respectively, and the 2nd harmonic frequencies are illustrated in green and magenta vertical dash-dotted lines respectively.

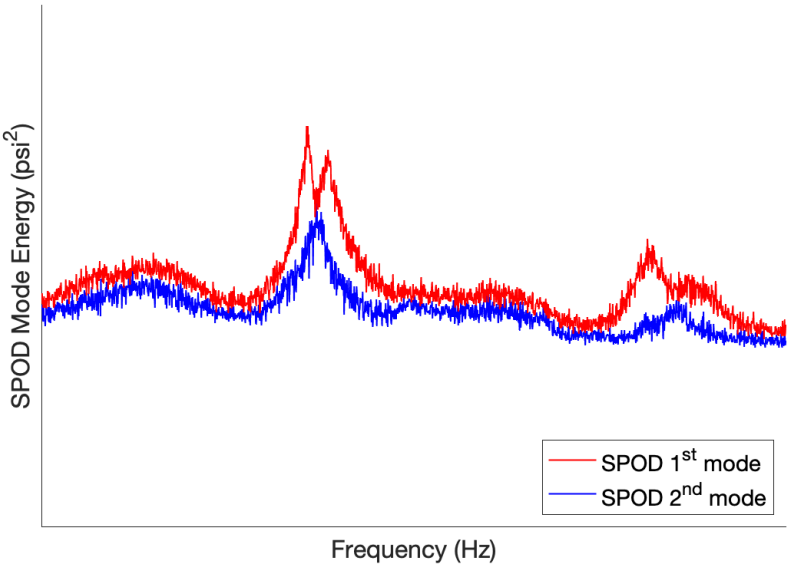


(a)

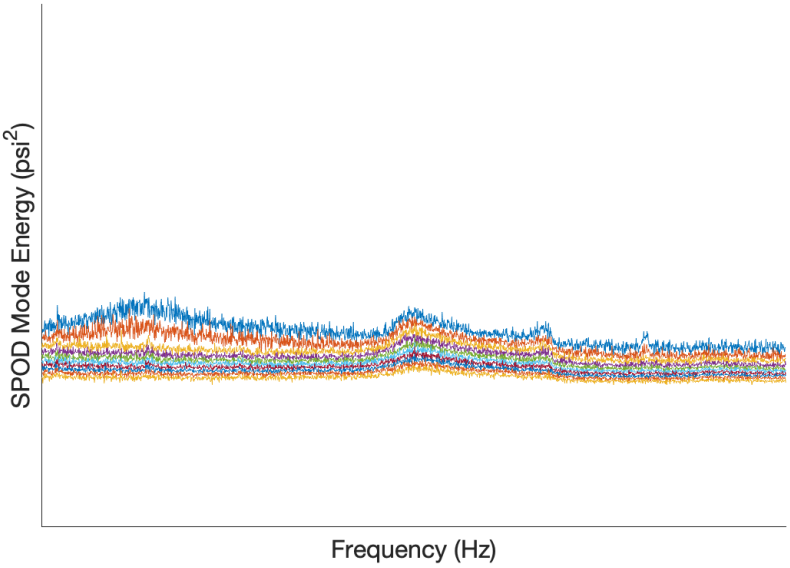


(b)

**Figure 6.** Energy of SPOD modes of two sets of timeseries of vortex shedding tones (a) and broadband signals (b) separated from the original uPSP measurements on the selected grid nodes in the supersonic test at Mach number 1.20 of the SLS Force & Moment Test as the function of frequency in the interested frequency band.

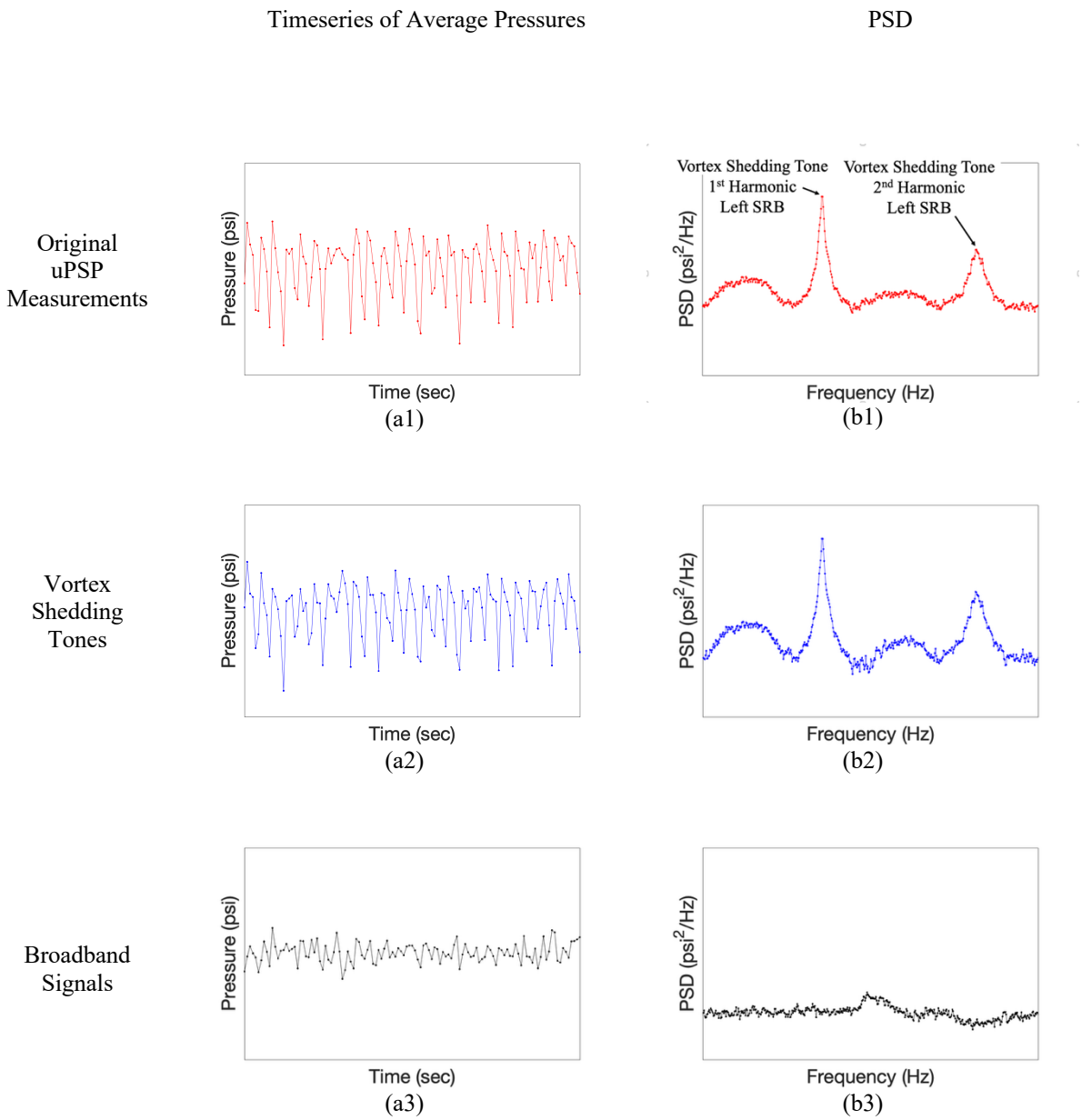


**Figure 7.** Timeseries of average pressures (a1, a2, a3) on the reference patch and the corresponding PSDs (b1, b2, b3) as the function of frequency in the interested frequency band, generated from three datasets of original uPSP measurements (a1, b1), vortex shedding tones (a2, b2) and broadband signals (a3, b3).

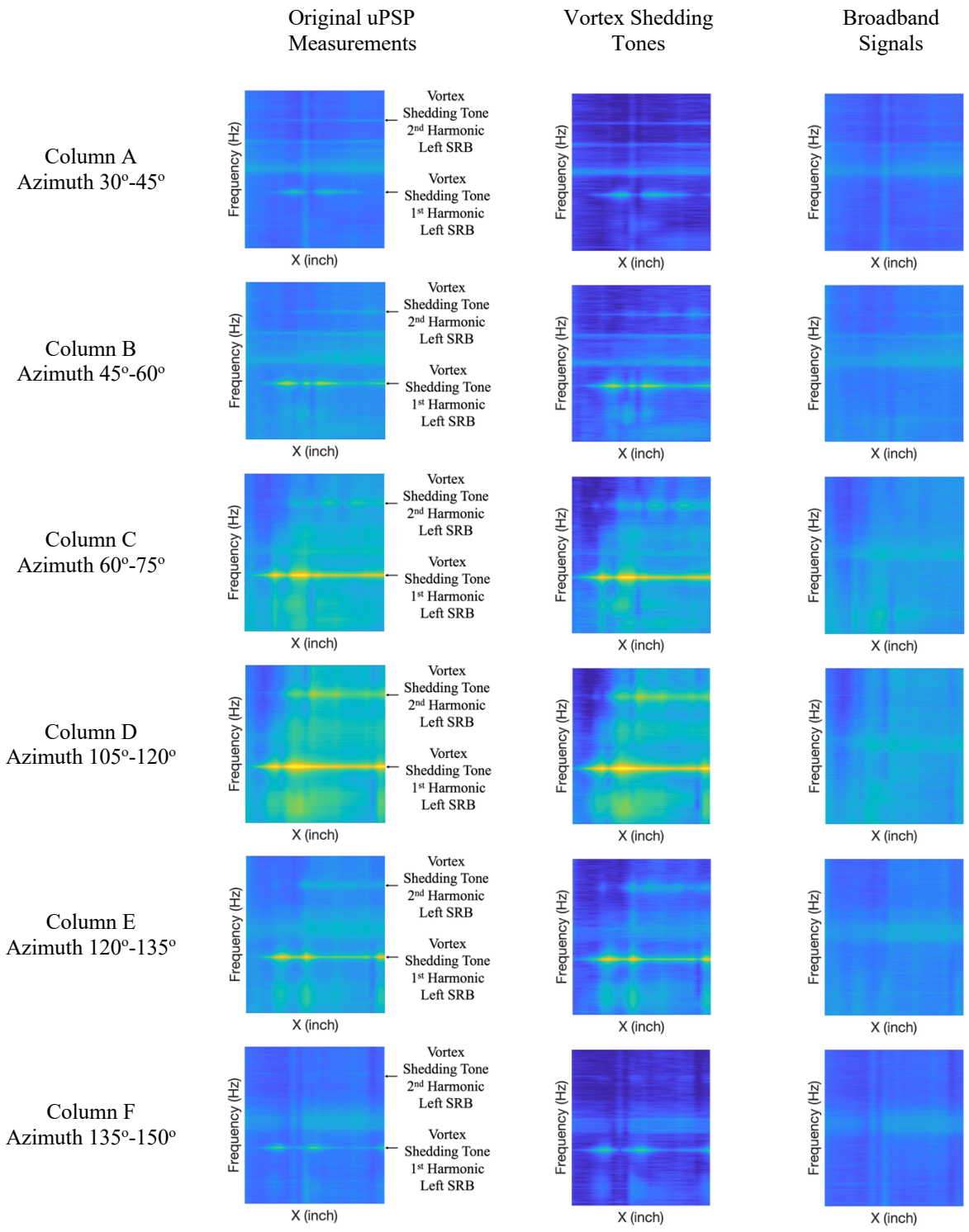


**Figure 8.** Spectrograms of timeseries of average pressures on patches, generated from three datasets of original uPSP measurements (1st column), vortex shedding tones (2nd column) and broadband signals (3rd column). Rows 1-6 show the spectrograms of timeseries of average pressures on the patches in Columns A, B, C, D, E and F, respectively, in the group of left SRB.

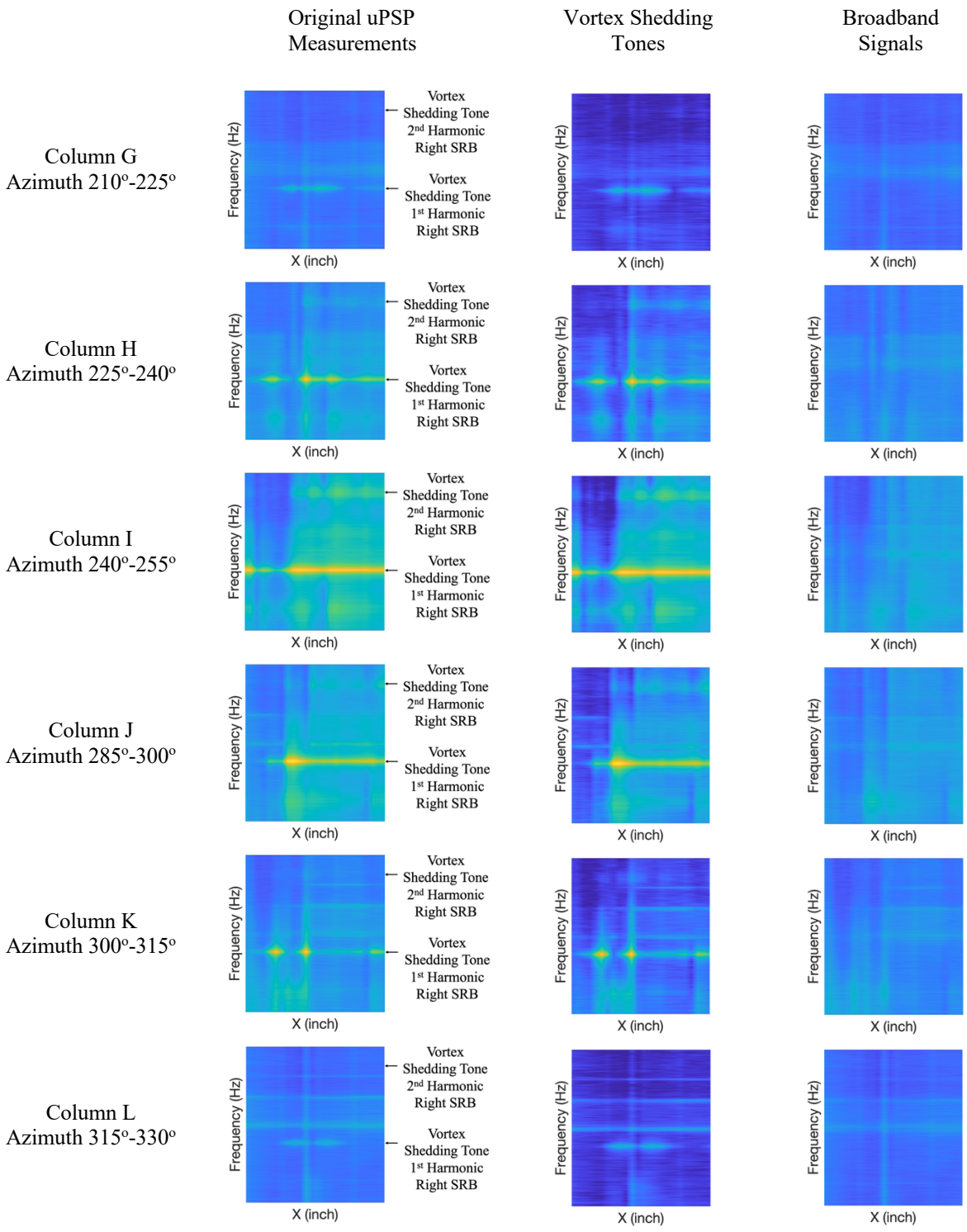


**Figure 9.** Spectrograms of timeseries of average pressures on patches, generated from three datasets of original uPSP measurements (1st column), vortex shedding tones (2nd column) and broadband signals (3rd column). Rows 1-6 show the spectrograms of timeseries of average pressures on the patches in Columns G, H, I, J, K and L, respectively, in the group of right SRB.

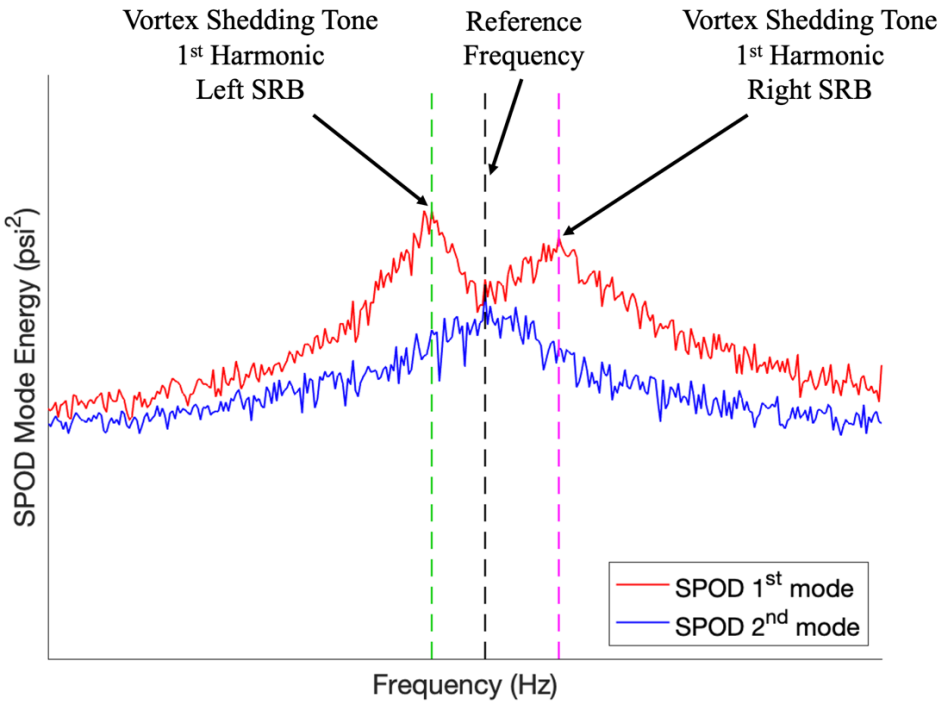


**Figure 10.** Energy of two SPOD modes of the dataset of the separated vortex shedding tones in the supersonic test at Mach number 1.20 of the SLS Force & Moment Test as the function of frequency. Compared to Fig. 6(a), this figure focuses on a smaller frequency band. The 1st harmonic frequencies of the vortex shedding tones of the left and right SRBs are illustrated in the green and magenta vertical dash lines, respectively. The reference frequency is illustrated in the black vertical dash line.

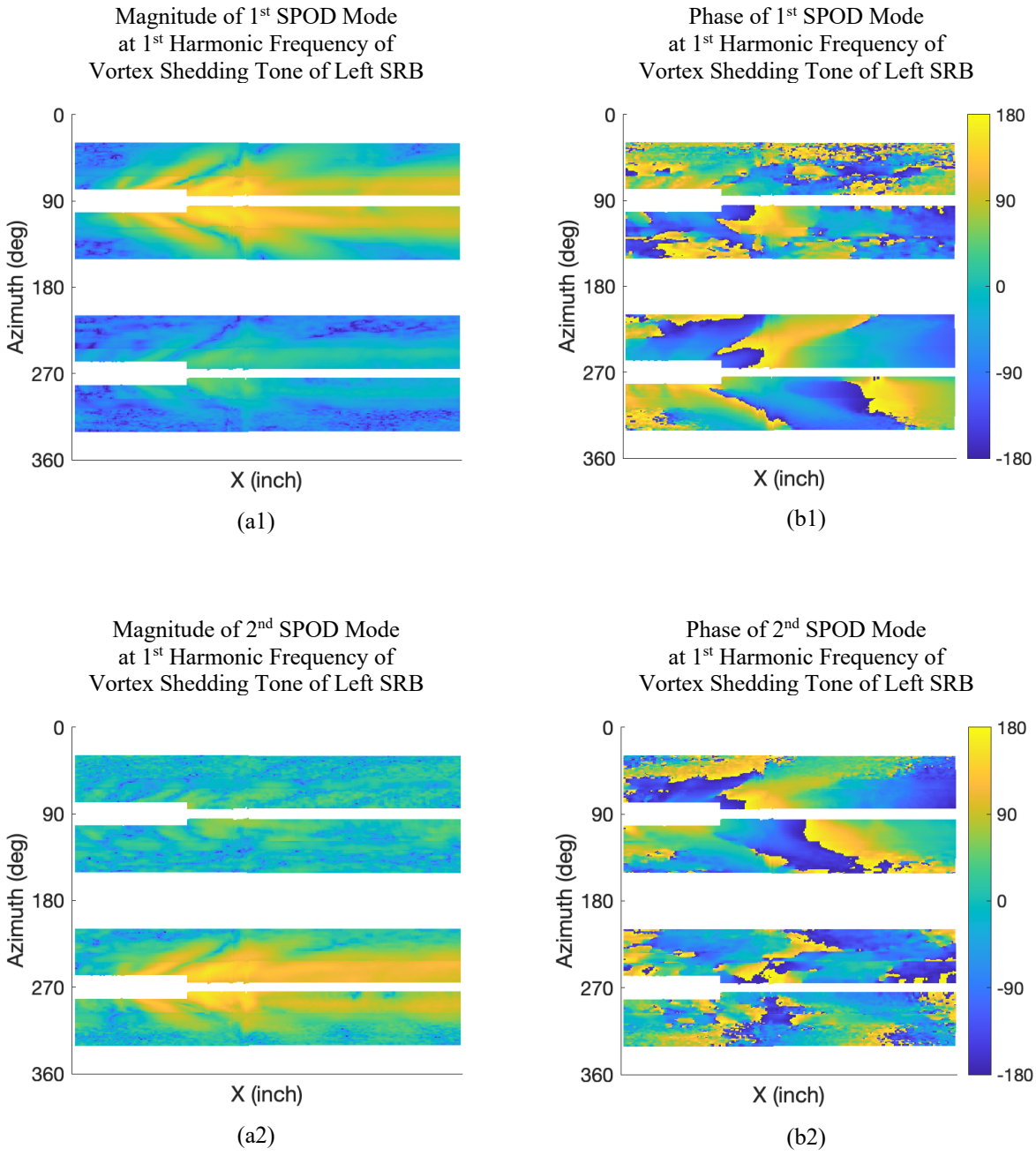


**Figure 11.** Magnitudes (a1, a2) and phases (b1, b2) of the 1st (a1, b1) and 2nd (a2, b2) SPOD modes of the dataset of vortex shedding tones at the 1st harmonic frequency of the vortex shedding tone of the left SRB in the supersonic test at Mach number 1.20 of the SLS Force & Moment Test, plotted on the plane of the X-coordinate and azimuth of the nodes. Note the azimuth ranges from 0° to 360°.

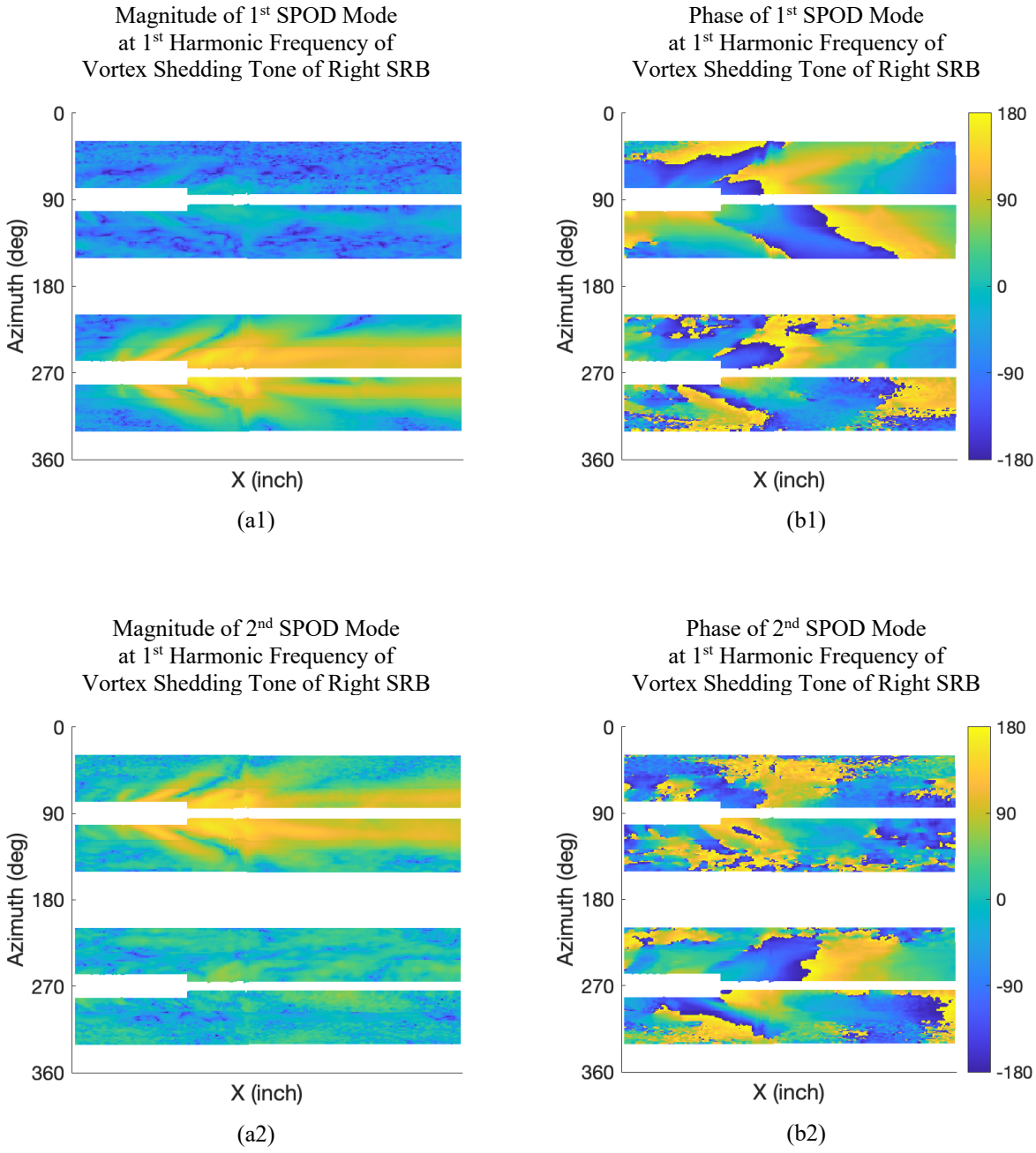


**Figure 12.** Magnitudes (a1, a2) and phases (b1, b2) of the 1st (a1, b1) and 2nd (a2, b2) SPOD modes of the dataset of vortex shedding tones at the 1st harmonic frequency of the vortex shedding tone of the right SRB in the supersonic test at Mach number 1.20 of the SLS Force & Moment Test, plotted on the plane of the X-coordinate and azimuth of the nodes. Note the azimuth ranges from 0° to 360°.

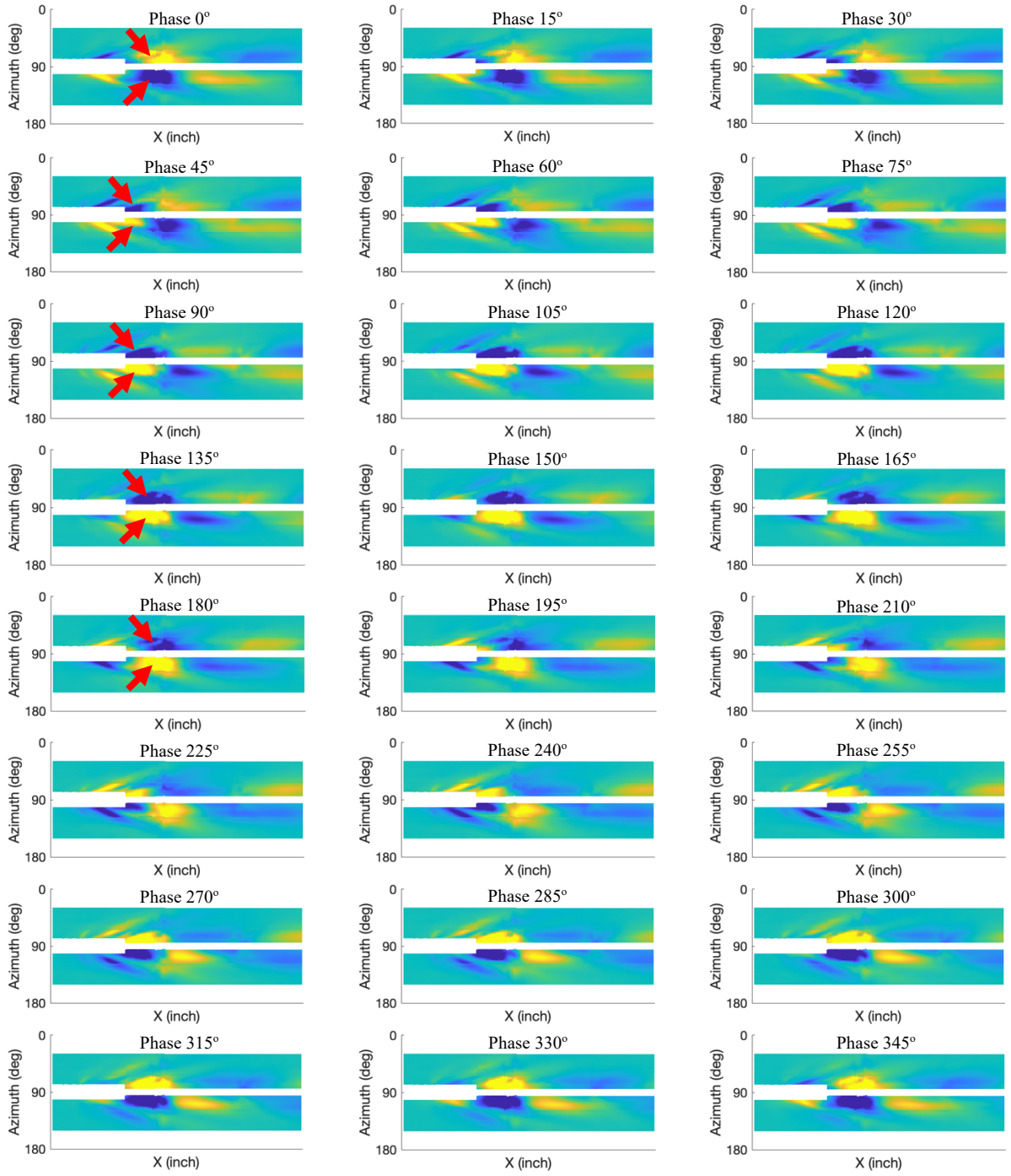


**Figure 13.** 1st SPOD mode of the dataset of vortex shedding tones at the 1st harmonic frequency of the vortex shedding tone of the left SRB at phases 0° through 345° in increments of 15° in time domain in the supersonic test at Mach number 1.20 of the SLS Force & Moment Test, plotted on the plane of the X-coordinate and azimuth of the nodes. Note the azimuth ranges from 0° to 180°.

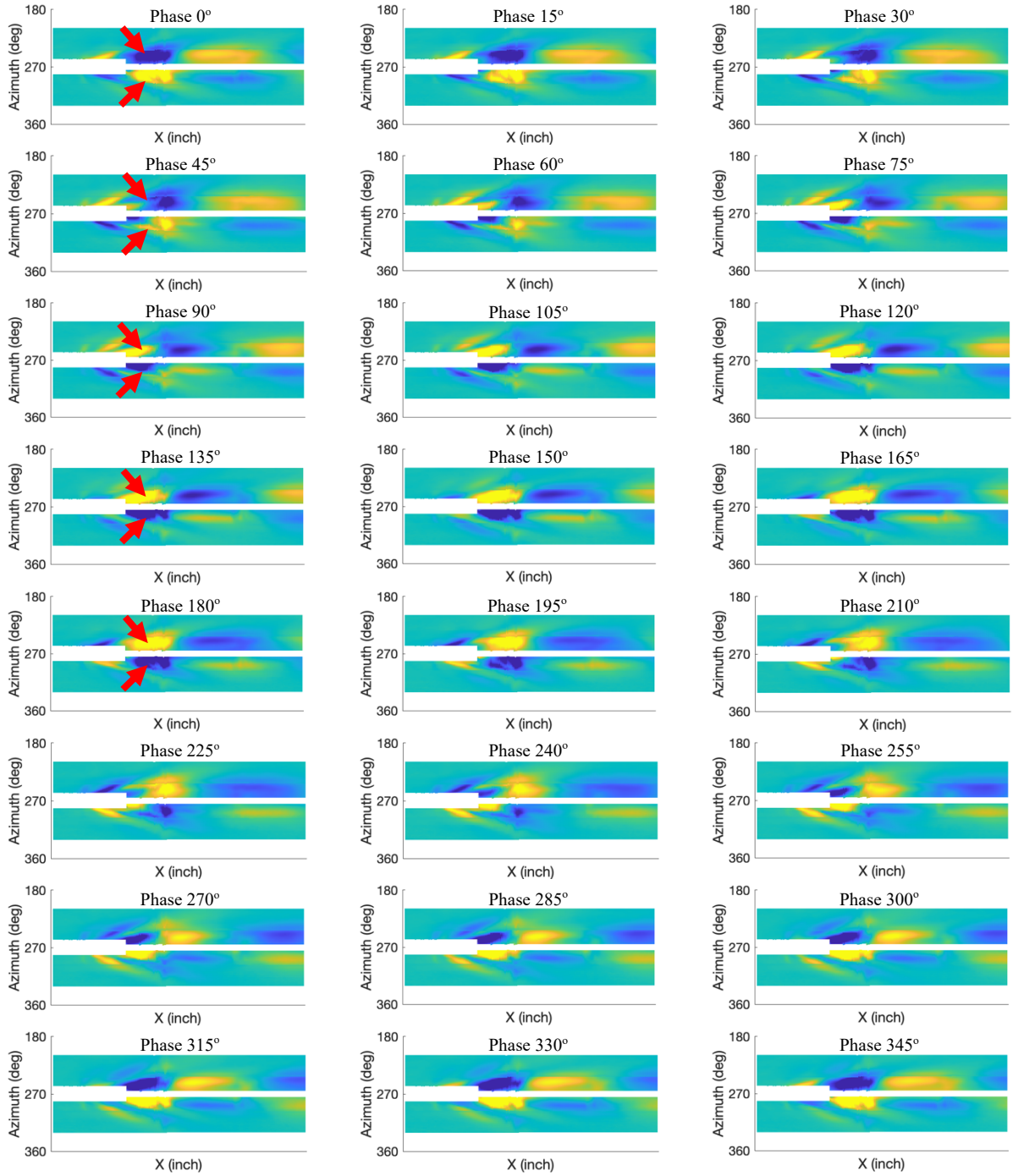


**Figure 14.** 1st SPOD mode of the dataset of vortex shedding tones at the 1st harmonic frequency of the vortex shedding tone of the right SRB at phases 0° through 345° in increments of 15° in time domain in the supersonic test at Mach number 1.20 of the SLS Force & Moment Test, plotted on the plane of the X-coordinate and azimuth of the nodes. Note the azimuth ranges from 180° to 360°.

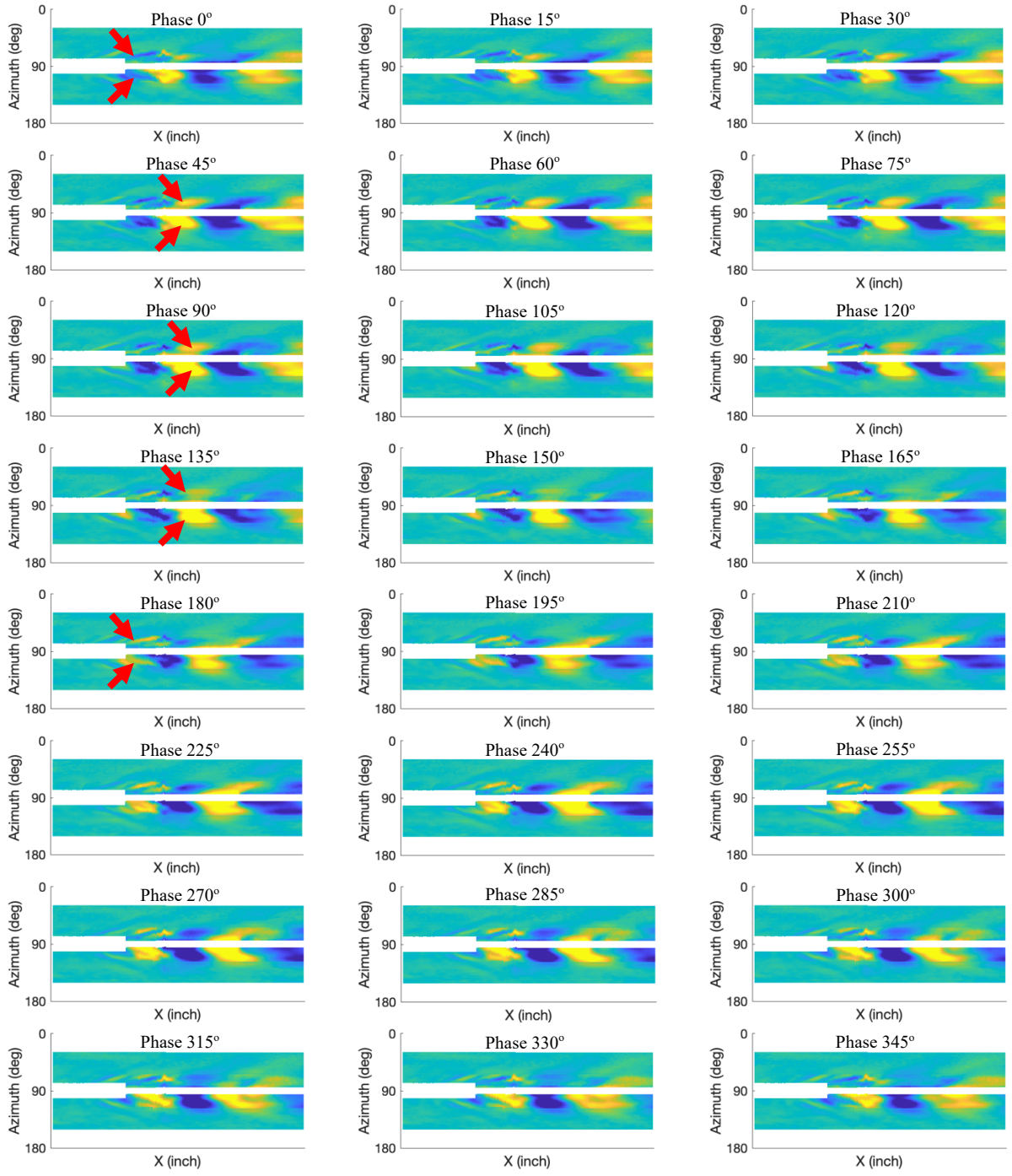


**Figure 15.** 1st SPOD mode of the dataset of vortex shedding tones at the 2nd harmonic frequency of the vortex shedding tone of the left SRB at phases 0° through 345° in increments of 15° in time domain in the supersonic test at Mach number 1.20 of the SLS Force & Moment Test, plotted on the plane of the X-coordinate and azimuth of the nodes. Note the azimuth ranges from 0° to 180°.

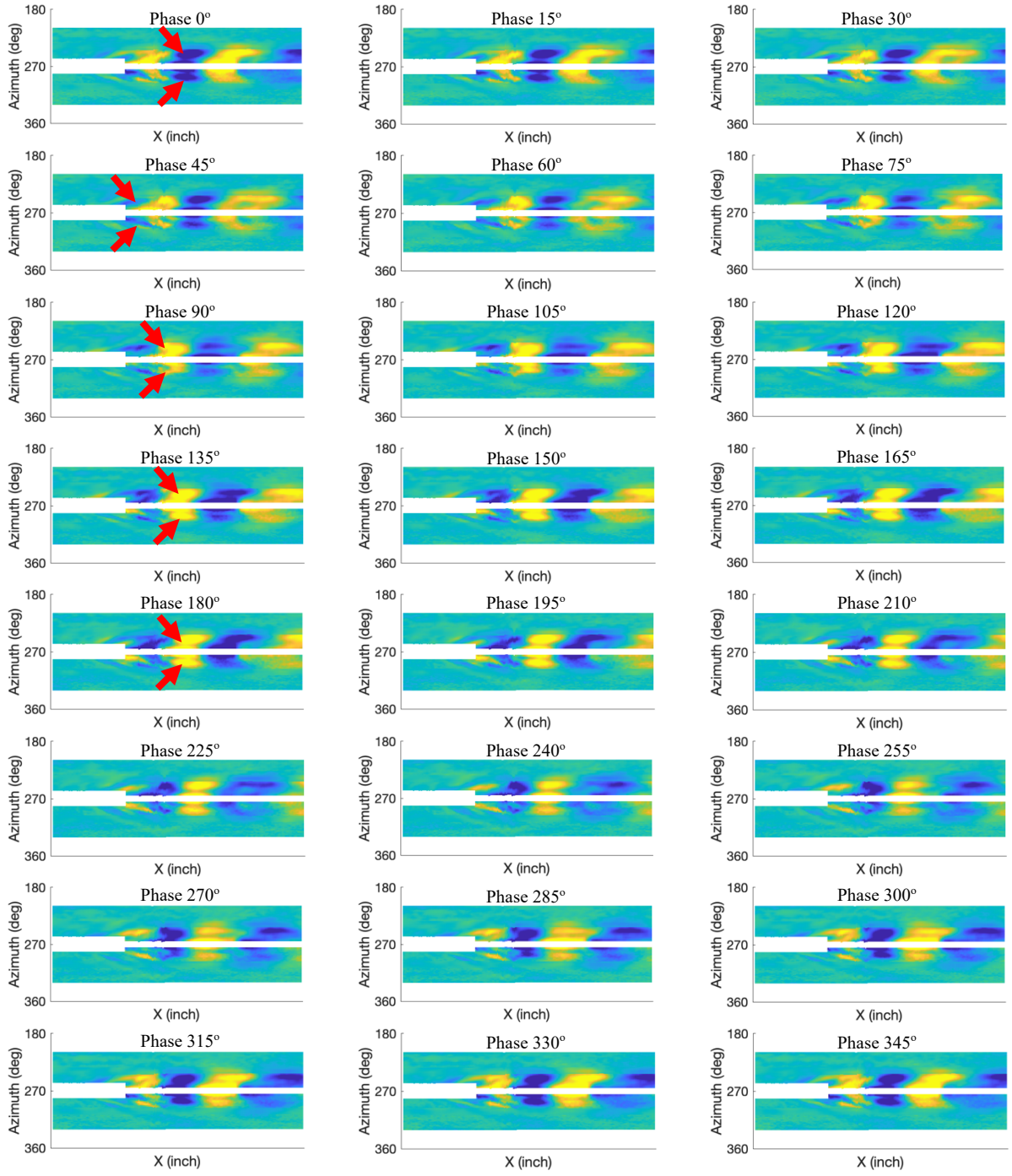


**Figure 16.** 1st SPOD mode of the dataset of vortex shedding tones at the 2nd harmonic frequency of the vortex shedding tone of the right SRB at phases 0° through 345° in increments of 15° in time domain in the supersonic test at Mach number 1.20 of the SLS Force & Moment Test, plotted on the plane of the X-coordinate and azimuth of the nodes. Note the azimuth ranges from 180° to 360°.